Hindawi
Geofluids
Volume 2023, Article ID 3380389, 14 pages
https://doi.org/10.1155/2023/3380389

*Research Article*

# Controlling Factors of Organic-Rich Lacustrine Shale in the Jurassic Dongyuemiao Member of Sichuan Basin, SW China

**Yadong Zhou,[1,2,3] Chan Jiang,[4] Dongfeng Hu,[5] Zhihong Wei,[5] Xiangfeng Wei,[5] Daojun Wang,[5] Jingyu Hao,[5] Yuqiang Jiang,[1,2,3] and Yifan Gu[1,2,3]**

[1]*School of Geosciences and Technology, Southwest Petroleum University, Chengdu 610500, China*
[2]*The Unconventional Reservoir Evaluation Department, PetroChina Key Laboratory of Unconventional Oil and Gas Resources, Chengdu 610500, China*
[3]*Collaborative Innovation Center of Shale Gas Resources and Environment, Chengdu 610500, China*
[4]*Exploration Division, PetroChina Southwest Oil and Gas Field Company, Chengdu 610041, China*
[5]*Sinopec Exploration Company, Chengdu 610041, China*

Correspondence should be addressed to Yifan Gu; xnsygyf@126.com

Received 23 December 2022; Revised 13 June 2023; Accepted 24 July 2023; Published 11 October 2023

Academic Editor: Hexin Huang

Copyright © 2023 Yadong Zhou et al. This is an open access article distributed under the Creative Commons Attribution License, which permits unrestricted use, distribution, and reproduction in any medium, provided the original work is properly cited.

Organic-rich continental shale, widespread in the Sichuan Basin during the deposition of the Jurassic Dongyuemiao Member ($J_1$d), is considered the next shale hydrocarbon exploration target in southern China. To identify a shale gas sweetspot and reduce exploration risk, it is of great significance to determine the organic matter (OM) enrichment mechanism of $J_1$d shale. In this study, based on sedimentological characteristics and organic matter content, high-resolution major and trace elements were systematically analyzed to demonstrate terrigenous influx, paleoredox, paleosalinity, paleoproductivity, and paleoclimate. The 1st section interval of the $J_1$d 1st submember is dominated by shallow lake subfacies, while the other intervals have the characteristic of semideep to deep lake subfacies. The 1st submember interval of $J_1$d lacustrine shale is characterized by the warmest-humid paleoclimate, strongest weathering degree, highest terrigenous input, moderate paleoproductivity, and paleoredox condition. Within the Dongyuemiao 1st submember, the 4th section interval has the highest paleoproductivity and the most oxygen-deficient condition in bottom water. During the deposition period of the 2nd submember, the sedimentary environment turned to a cold-dry paleoclimate, weak weathering degree, low terrigenous input, low paleosalinity, and high paleoproductivity. Under the background of semideep and deep lake, the terrigenous OM input plays the most critical role in controlling OM enrichment. Moreover, the high primary productivity of lake surface water and the suboxic condition of lake bottom water contribute to the formation of relatively higher TOC lacustrine shale interval in the 4th section of 1st submember.

## 1. Introduction

Organic-rich shales are widely deposited under the following sedimentary environments: deep shelf, semideep and deep lacustrine, estuary bay, and lagoon environment [1–4]. In North America, the huge commercial success has been achieved in marine shale exploration [5–8]. In China, several trillion cubic meters-scale shale gas fields, such as Fuling, Weirong, and Zhaotong, have been successively built around the Sichuan Basin [9, 10]. However, these successful shale hydrocarbon exploration cases are limited to the marine organic-rich shale [11–13].

Previous studies have revealed that lacustrine shale in China has great exploration potential, and corresponding mechanismic investigations have been carried out in the Jurassic strata of the Sichuan Basin, Triassic Yanchang Fm. in Ordos Basin, Shahejie Fm. of Bohai Bay Basin, Cretaceous Shahai and Jiufotang Fm. in Fuxin Basin, and the Cretaceous Qingshankou Fm. of Songliao Basin [14–16]. The Jurassic continental shale strata in the

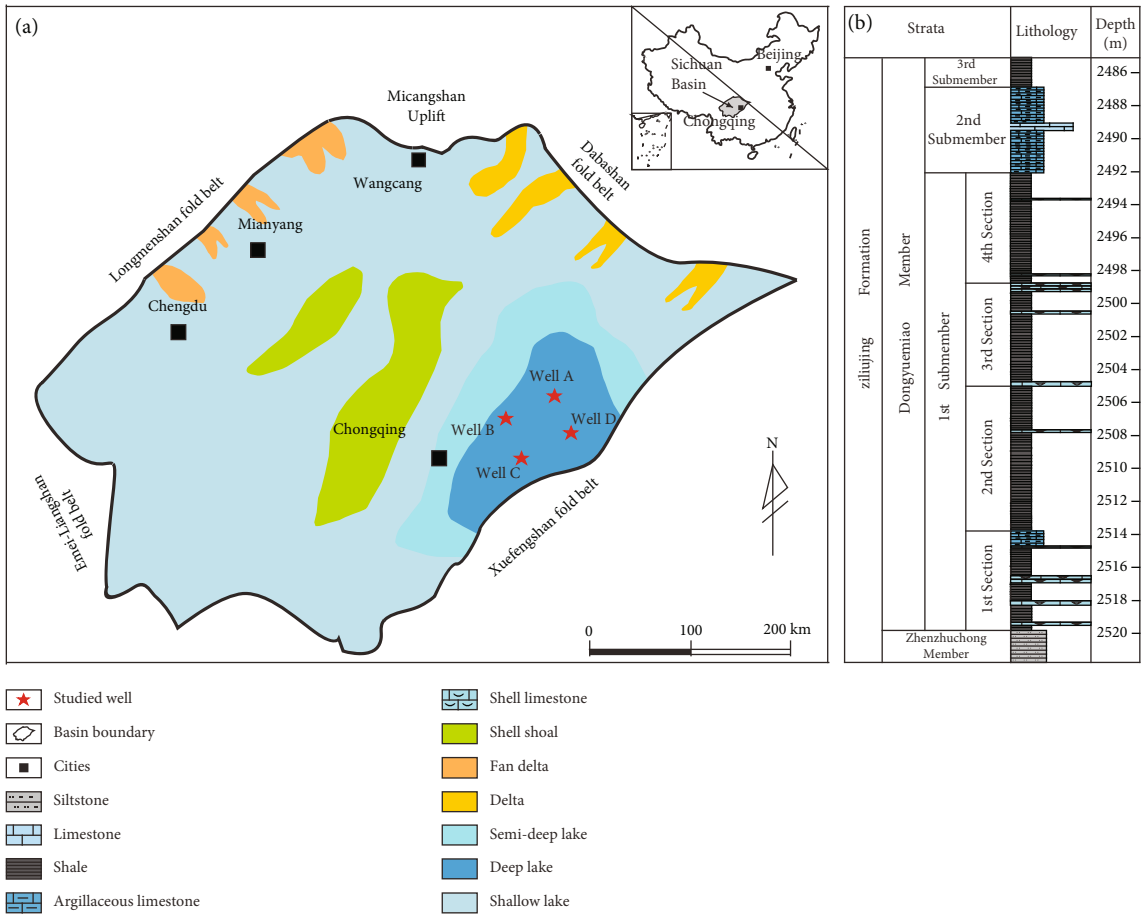


FIGURE 1: (a) Sedimentary facies during the Jurassic Dongyuemiao member ($J_1d$) deposition, Sichuan Basin (modified from [21]). (b) Generalized stratigraphy of the Jurassic Dongyuemiao member ($J_1d$) in Eastern Sichuan Basin (well B).

Sichuan Basin are considered the most realistic alternative exploration target [16, 17]. In order to achieve efficient exploration and development, it is first necessary to identify the "sweetspots" of lacustrine organic-rich shale. Nevertheless, the sedimentary characteristics and organic matter accumulation mechanism have yet to be unified.

Elemental proxies have been applied very often to reveal environmental effect including terrigenous input, paleoredox condition, paleosalinity, and paleoproductivity on the accumulation of organic matter in fine-grained sedimentary rocks [3, 4]. Based on the division of Dongyuemiao Member in the Sichuan Basin, sedimentary facies marker, petrological characterization, and high-resolution elemental analyses are integrated to determine environmental conditions of different intervals in Dongyuemiao lacustrine shale. This study is aimed at deepening understanding of origin of Dongyuemiao lacustrine organic-rich shale and provide guidance for shale gas development.

## 2. Geological Background

The Sichuan Basin is a typical craton basin at the western Upper Yangtze Block (Figure 1(a)), and the basin area is about 260,000 $km^2$. The study area is located in the Eastern Sichuan Basin (Figure 1(a)), dominated by lacustrine environment during the Early to Middle Jurassic. The Dabashan, Longmenshan, and Micangshan on the periphery of the basin constitute the provenance areas of the Jurassic sedimentary period [17–19]. Four times lake transgressions were identified during Jurassic system. From the bottom to the top, four continental shale strata are identified: Zhenzhuchong Member ($J_1z$), Dongyuemiao Member ($J_1d$), Da'anzhai Member ($J_1dn$), and Lianggaoshan Fm. ($J_1l$), respectively. OM is thought to accumulate in semideep lacustrine to deep lacustrine environment controlled by anoxic condition [18, 19]. The lithology of $J_1d$ is mainly shale, followed by shale limestone and argillaceous limestone. Three submembers can be identified based on lithology: 1st submember, 2nd submember, and 3rd submember. The 1st submember can be subdivided into four sections: 1st, 2nd, 3rd, and 4th sections (Figure 1(b)). Except for the 2nd submember, the other intervals mainly constitute shale. The total organic carbon (TOC) value of $J_1d$ shale is between 0.5% and 2.0%, and the average value is greater than 1% [20]. The OM type is mainly type II and locally developed type III, and the vitrinite reflectance ($R_o$) exceeds 1.2%. Thus, it has entered the stage of high-maturity evolution and is during gas generation stage.

## 3. Samples and Methods

*3.1. Macroscopic and Microscopic Sedimentological Characteristics.* The four wells shown in Figure 1(a) were continuously cored in the $J_1$d. First, the macroscopic sedimentological characteristics of cores were observed. In order to observe the microscopic sedimentological characteristics, 200 thin sections from core samples were observed by the Carl Zeiss Imager 2 microscope.

*3.2. OM Content.* TOC were measured by the Exploration and Development Research Institute of CNPC, using Leco carbon/sulfur analyzer with ±0.5% in experimental error. Firstly, 150 samples were grind into powder, and then carbonate components were removed by 10% hydrochloric acid. The remaining samples were washed with pure water to neutral and then dried at 70°C-90°C. In order to realize the organic carbon combustion, dried powders were added to the cosolvent and sufficiently burned in high-temperature oxygen flow. Carbon dioxide formed by combustion was detected by infrared detector to obtain the TOC value.

*3.3. Major and Trace Element Concentration.* The major and trace element concentrations were acquired by X-ray fluorescence spectroscopy. Fifty-six core samples were grind into powder and then shaped to a suitable fused glass beads to fit the XRF spectrometer. The XRF intensity of major and trace elements were determined. Based on the calibration curve or equation, the interference effect between elements was corrected, and the element content was obtained. The test accuracy of major element content is less than 1%.

## 4. Results

*4.1. Sedimentological Characterization*

*4.1.1. Shallow Lacustrine Subfacies.* Shallow lacustrine subfacies refer to the zone between lakeside and wave base. According to the difference of sediment and hydrodynamic conditions, it can be subdivided into two microfacies: shell shoal and intershoal mud. The matrix of shallow lacustrine sediments is composed of terrigenous clay minerals (Figure 2(a)). Shell fragments can be identified on the core surface with volumetric content over 50% (Figures 2(b) and 2(c)). Within intershoal mud microfacies (Figure 2(d)), it has characteristics of ripple bedding and parallel bedding (Figure 2(e)), and reflecting large fluctuation energy of lake water (Figure 2(f)). Silt laminae consist of silts or silt-size clasts derived from lakeshore environment (Figure 2(g)). The 1st section of $J_1$d shale belongs to shallow lacustrine subfacies (Figure 3).

*4.1.2. Semideep Lacustrine Subfacies.* The semideep lacustrine subfacies are located below the wave-base level and above-the-storm-wave base level. Within subfacies, sediments are mainly affected by lake currents, not by waves. The rock types of semideep lacustrine subfacies are mainly gray-black shale (Figure 4(a)). Under the influence of slope and gravity, abundant sedimentary characteristics of gravity flow origin can be observed in semideep lacustrine subfacies (Figure 4(b)), including cohesive debris flow (CDF) and low-density turbidity current (LTC) (Figure 4(c)). Different from the normally stacked shell fragments in the shell shoal, the shell fragments inside the CDF are tightly squeezed to form massive bedding (Figure 4(e)). LTC is typically characterized by graded bedding, and multiple graded beddings overlay upward in the vertical direction (Figure 4(c)). Occasionally, erosional surfaces can be observed at the bottom of each graded bedding (Figure 4(f)). In addition to CDF and LTC, transitional flow deposits associated with LTC and CDF can also be identified [22–24]. The transitional flow deposits internally exhibit frequent interbedding of discontinuous lenticular siltstone (or shell fragments) and matrix shale (Figure 4(g)).

*4.1.3. Deep Lacustrine Subfacies.* Deep lacustrine subfacies refer to the deepest part of lake. Wave can hardly affect this subfacies, so the sedimentary water is quiet, and the stratification of the water body forms an dysoxic-suboxic environment of the bottom water. Benthos cannot survive in this environment, so no shell fragments are observed on core surface (Figure 5(a)). The rock type of this subfacies is gray-black shale (Figure 5(b)). The laminae inside the shale are not obvious and the boundaries of each laminae (Figure 5(c)). The terrigenous influx in the deep lacustrine subfacies is very small (Figure 5(d)). The terrigenous debris is mainly composed of silt-size quartz particles (Figure 5(e)), which are dispersed in the shale (Figure 5(f)), and the bedding and orientation are poor (Figure 5(g)). Since the extremely low terrigenous influx weakens the dilution effect of terrigenous debris on organic matter, organic matter can be well enriched.

*4.2. TOC Content.* Results suggest that the content of the 1st section lacustrine shale has a wide range, from 0.93% to 2.27% (Figure 3), averaging 1.57% ($n = 8$). For the 2nd section lacustrine shale, the range of TOC is 1.05%-2.37%, with an average of 1.74% ($n = 13$). In the 3rd section lacustrine shale, the range of TOC is 1.20%-2.51%, averaging 1.70% ($n = 10$). The TOC range of lacustrine shale for the 4th section is relatively higher than the other sections, ranging from 1.25% to 4.03%; the average value is 2.25% ($n = 10$). The TOC of the 2nd submember argillaceous limestone and calcareous mudstone varies narrowly, from 0.52% to 1.44%, averaging 1.07% ($n = 12$). For the 3rd submember lacustrine shale, the range of TOC is 0.98%-1.45%, averaging 1.21% ($n = 3$).

*4.3. Major Element Concentration.* As shown in Figure 6, the Ca concentration of the 1st section lacustrine shale varies widely, from 0.36% to 19.09%, averaging of 5.02% ($n = 8$). For the 2nd section lacustrine shale, the content of Ca is between 0.20% and 21.80%, averaging 5.12% ($n = 13$). The Ca concentration of the 3rd section lacustrine shale varies narrowly, ranging from 0.24% to 4.62%, averaging 1.60% ($n = 10$). The Ca content of 4th section lacustrine shale varies widely, ranging from 0.12% to 22.08%, with an average of 5.73% ($n = 10$). The content of Ca for 1st submember is close to the upper continental crust.

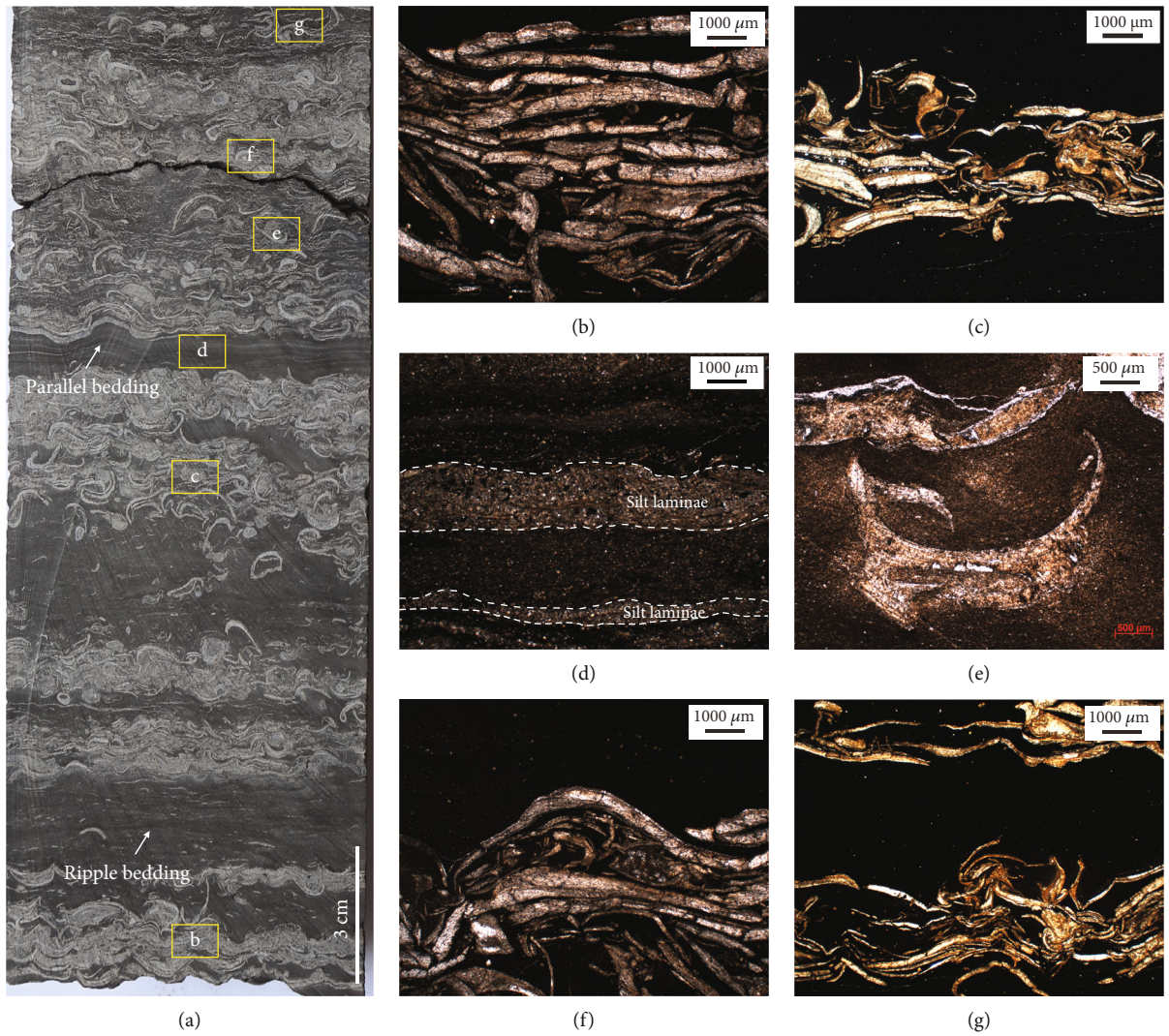


FIGURE 2: Macroscopic and microscopic sedimentary characteristics of shallow lacustrine subfacies for $J_1d$ from well A. (a) Core photograph of shallow lacustrine subfacies showing shell shoal and ripple bedding, 1 section, 2518.29 m-2518.50 m. (b) Normal stack of shell fragments, 2518.49 m. (c) Normal stack of shell fragments exhibiting wave fluctuation, 2518.39 m. (d) Silt laminae showing discontinuous planar lamination, 2518.36 m. (e) Shell fragments exhibiting strong wave fluctuation, 2518.34 m. (f) Normal stack of shell fragments, 2518.32 m. (g) Normal stack of shell fragments, 2518.29 m.

The content of Ca for 2nd submember argillaceous limestone and calcareous mudstone is higher than the other sections and the upper continental crust, ranging from 2.92% to 25.54%, with average value of 15.10% ($n = 12$). The Ca concentration of 3rd Submember lacustrine shale varies narrowly ($n = 3$), from 4.25% to 6.85%, averaging 5.83%.

The Al content and Si content of the 1st submember lacustrine shale are relatively higher (Figure 6). The average concentration of Al and Si is 10.19% (3.51%-12.20%, $n = 41$) and 22.54% (9.74%-27.86%, $n = 41$), respectively. The content of Al is higher than that of the upper continental crust, while Si is lower than that of the upper continental crust. The average concentration of Al and Si in 2nd submember lacustrine shale is 6.59% (3.16%-11.82%, $n = 12$) and 14.92% (8.37%-23.18%, $n = 12$), respectively. The average concentration of Al and Si for 3rd submember lacustrine shale is 9.13% (8.52%-10.32%, $n = 3$) and 23.42% (22.58%-24.16%, $n = 3$), respectively.

The average concentration of Ti and Zr in the 1st submember lacustrine shale is 4765 ppm (1793 ppm-6138 ppm, $n = 41$) and 144 ppm (47 ppm-1997 ppm, $n = 41$), respectively. The average concentration of Ti and Zr for 2nd submember lacustrine shale is 2380 ppm (1067 ppm-4691 ppm, $n = 12$) and 81 ppm (38 ppm-138 ppm, $n = 12$), respectively. The average concentration of Ti and Zr for 3rd submember lacustrine shale is 3831 ppm (3491-4126 ppm, $n = 3$) and 137 ppm (128 ppm-153 ppm, $n = 3$), respectively.

*4.4. Trace Element Concentration.* The variation of environment-sensitive trace elements and elemental indicators is shown in Figures 7 and 8. Compared to the other two submembers, the CIA* for 1st submember lacustrine shale is higher, ranging from 18.83 to 85.20, averaging 70.64 ($n = 41$). The CIA* of the 2nd submember lacustrine shale is the lowest (16.74-76.57), averaging 36.77 ($n = 12$). The CIA* for 3rd submember lacustrine shale ranges from

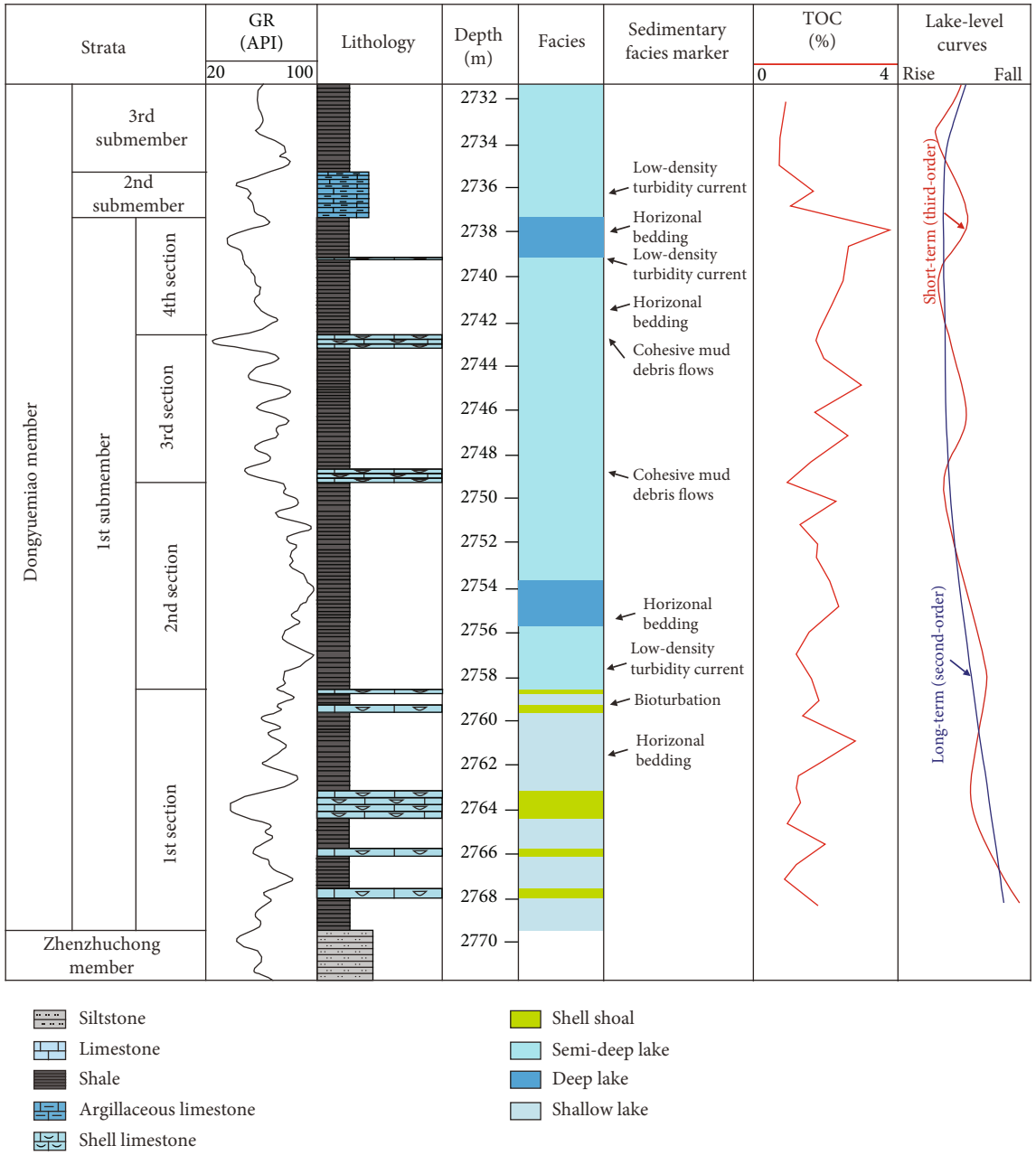


FIGURE 3: Integrated sedimentary column of $J_1d$ from the well B in the Eastern Sichuan Basin (the lake-level curves is modified from [19]).

57.60 to 69.68, with an average of 62.11 ($n = 3$). The range of PIA* is close to the CIA*.

The variation trend for V/Sc is contrary to that of the CIA* value (Figure 8). Specifically, the V/Sc for 1st submember lacustrine shale is relatively lower, ranging from 4.36 to 9.87, averaging 7.56 ($n = 41$). For the 2nd submember, the V/Sc is the highest, ranging between 6.42 and 9.83, averaging 8.28 ($n = 12$). The V/Sc of the 3rd submember lacustrine shale ranges from 7.48 to 8.05, averaging 7.85 ($n = 3$).

The variation of B/Ga is opposite to that of V/Sc (Figure 8). The B/Ga of the 1st submember lacustrine shale is the highest, ranging from 1.57 to 3.57, and the average value is 2.33 ($n = 41$). The B/Ga of the 2nd submember is relatively low, ranging between 1.35 and 2.52, averaging 1.90 ($n = 12$). The B/Ga for 3rd submember lacustrine shale ranges from 2.03 to 2.44, with an average of 2.19 ($n = 3$).

## 5. Discussion

*5.1. Terrigenous Influx.* The concentrations of Zr, Ti, and Al in fine-grained sedimentary rocks are hardly affected by weathering or diagenesis, thus these elements are used to evaluate terrestrial input [27, 28]. Al only exists in the clay minerals of fine-grained sedimentary rocks, while Ti and Zr are mainly assigned to clay, sand, and silt particles composed of ilmenite, rutile, and augite [29, 30]. The terrigenous input proxies represented by Al, Ti, and Zr has gradually decreasing trend in the 1st submember (Figure 6). Terrigenous input

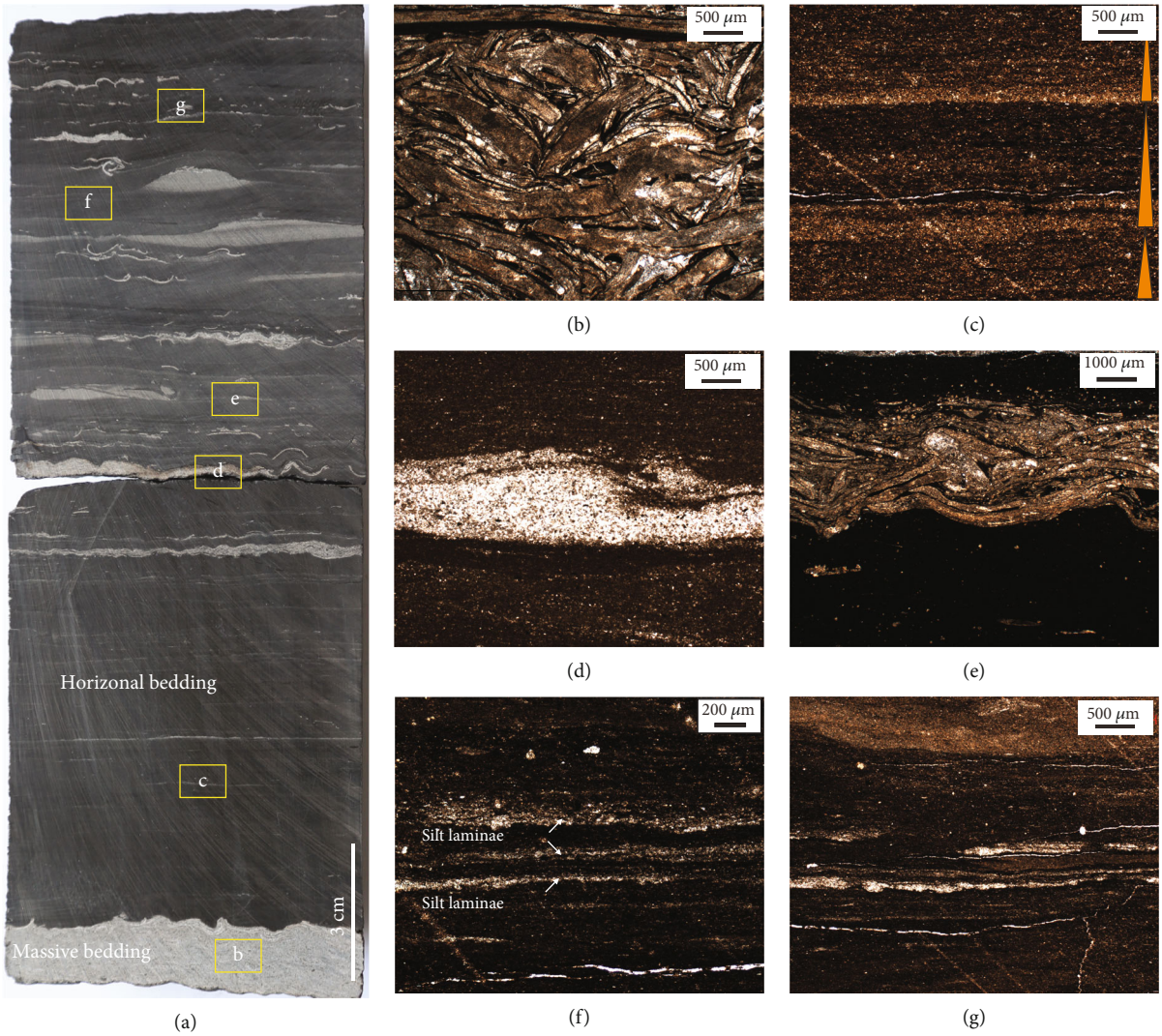


FIGURE 4: Macroscopic and microscopic sedimentary characteristics of semideep lacustrine subfacies for $J_1d$ from well A. (a) Core photograph of semideep lacustrine subfacies showing shell shoal and ripple bedding, 2nd section, 2492.19 m-2492.41 m. (b) Within cohesive debris flow deposit, shell fragments are tightly squeezed, 2492.4 m. (c) Multiple graded beddings overlay upward in the vertical direction, 2492.36 m. (d) Discontinuous lenticular siltstone, 2492.3 m. (e) Discontinuous lenticular silts and shell fragments, 2492.28 m. (f) Frequent interbedding of silt laminae and matrix shale, 2492.24 m. (g) Frequent interbedding of discontinuous silt laminae and matrix shale, 2492.21 m.

reaches lowest level in the 2nd submember. Into the 3rd submember, terrigenous input gradually increased. Zr/Al and Ti/Al ratios are thought to closely relate to the coarser part of sediments [29, 31]. The clear Ti-Al correlation suggests that Ti comes from the lattice of clay minerals or stable terrigenous clastic materials [3, 4]. The 1st-4th sections are characterized by clear Ti-Al correlation (Figure 9(a)), suggesting that the detrital influx is relatively stable. Zr usually exists in clay minerals or heavy minerals of silt size (e.g., zircons) [32]. The correlation of Al and Zr is clear in 1st-4th sections (Figure 9(b)). The results suggest that terrigenous influx for 1st-4th sections is relatively stable.

*5.2. Paleoclimate Conditions.* The warm-humid climate can contribute to the atmospheric water cycle by raising chemical weathering intensity. Under this environmental condition, nutrients are continuously transported to seawater or lake water, which helps to improve the primary productivity of surface water.

Chemical index of alteration (CIA) has been applied to determine paleoclimatic conditions. The specific calculation method is [33–35]

$$\mathrm{CIA}^{*} = 100 \times \frac{\mathrm{Al_2O_3}}{\mathrm{Al_2O_3} + \mathrm{Na_2O} + \mathrm{K_2O}}. \quad (1)$$

The enrichment factor (EF) of environment-sensitive trace elements has been widely applied to reveal environmental conditions.

The specific formula is as follows:

$$\mathrm{X_{EF}} = \frac{(X/\mathrm{Al})_{\mathrm{sample}}}{(X/\mathrm{Al})_{\mathrm{CC}}}. \quad (2)$$

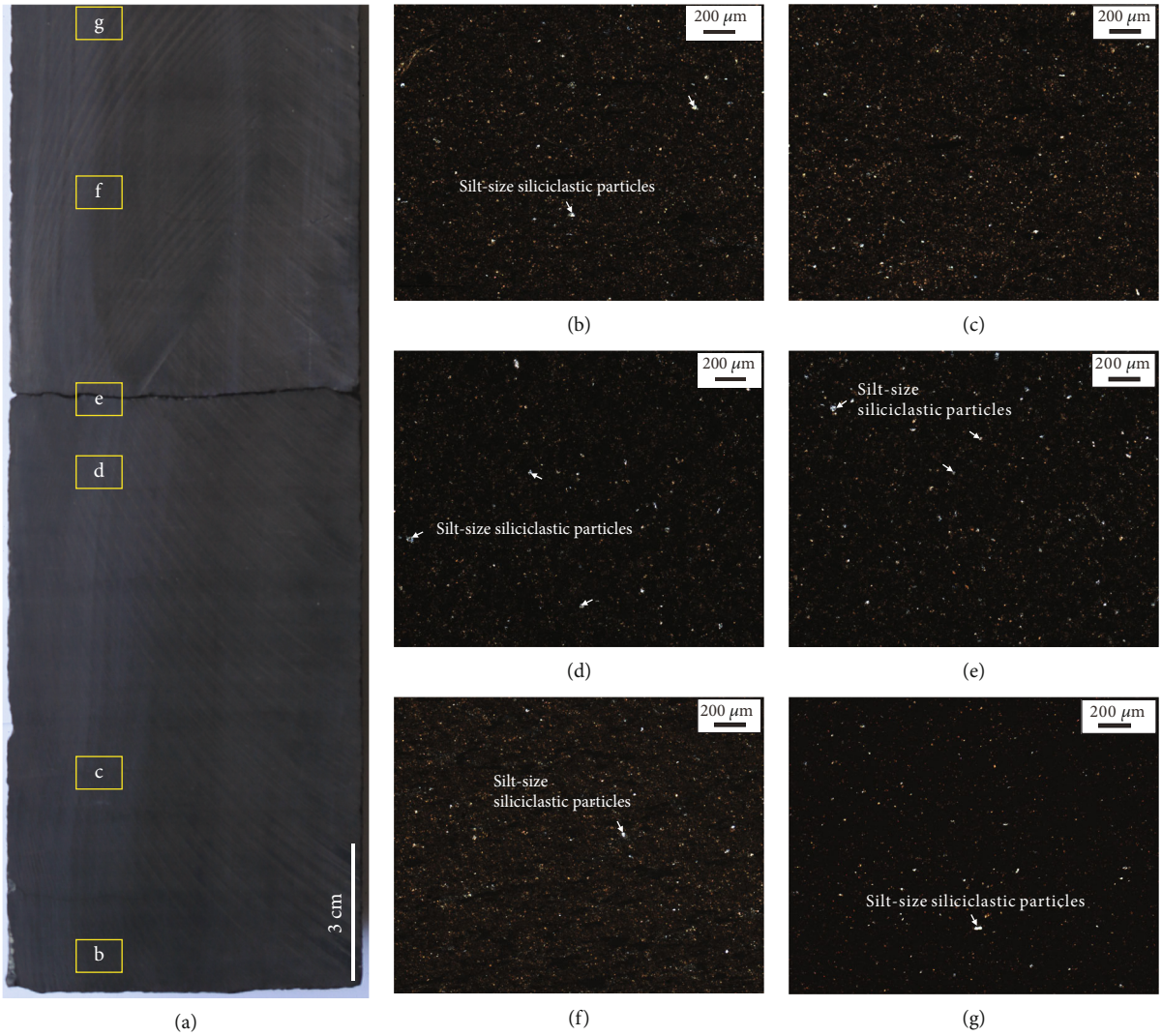


FIGURE 5: Macroscopic and microscopic sedimentary characteristics of deep lacustrine subfacies for $J_1d$ from Well A. (a) Gray-black shale, 2507.17 m-2507.39 m. (b) Fine-grained sediments including silt-size siliciclastic particles, 2507.38 m. (c) No laminae can be observed, 2507.34 m. (d) Fine-grained sediments including silt-size siliciclastic particles, 2507.28 m. (e) Fine-grained sediments including silt-size siliciclastic particles, 2507.26 m. (f) Fine-grained sediments including silt-size siliciclastic particles, 2507.21 m. (g) Fine-grained sediments including silt-size siliciclastic particles, 2507.18 m.

Note: X represents the element X concentration, and $((X/Al)_{CC}$ means the X/Al ratio in the continental crust [36–38].

Moreover, the excess value of element was another sensitive proxy reflecting environment condition [39]. The calculation formula is as follows:

$$X_{XS} = X_{total} - Ti_{total} \times \left(\frac{X}{Ti}\right)_{PAAS} \quad (3)$$

Note: $X_{total}$ represents the element $X$ concentration, and $X/Ti_{PAAS}$ means the X/Ti ratio in the Australian postarchean average shale (PAAS) [39].

Previous studies suggest that high CIA* values reflect warm, humid paleoclimate, and strong chemical weathering. And low CIA* values represent dry and cold conditions, and chemical weathering is weak [33, 40]. CIA* values ranging from 50 to 65 reflect cold-dry paleoclimate and low chemical weathering degree [40]. CIA* values ranging from 65 to 85 reflect the warm-humid paleoclimate and moderate chemical weathering. The CIA* values ranging from 85 to d 100 represent the hot and humid paleoclimatic condition with strong chemical weathering. The CIA* for the 1st submember is the highest, representing warm-humid climate. The CIA* for the 2nd submember is the lowest, reflecting relatively cold-dry climatic condition with low chemical weathering. The CIA* values of the 3rd submember are close to 1st submember, reflecting warm-humid climatic condition. The PIA* values for 1st submember are between 17 and 99, and the PIA* values for 2nd submember are between 15 and 50. The variation trend of the PIA* is similar to the CIA*, reflecting the same climate change (Figure 8).

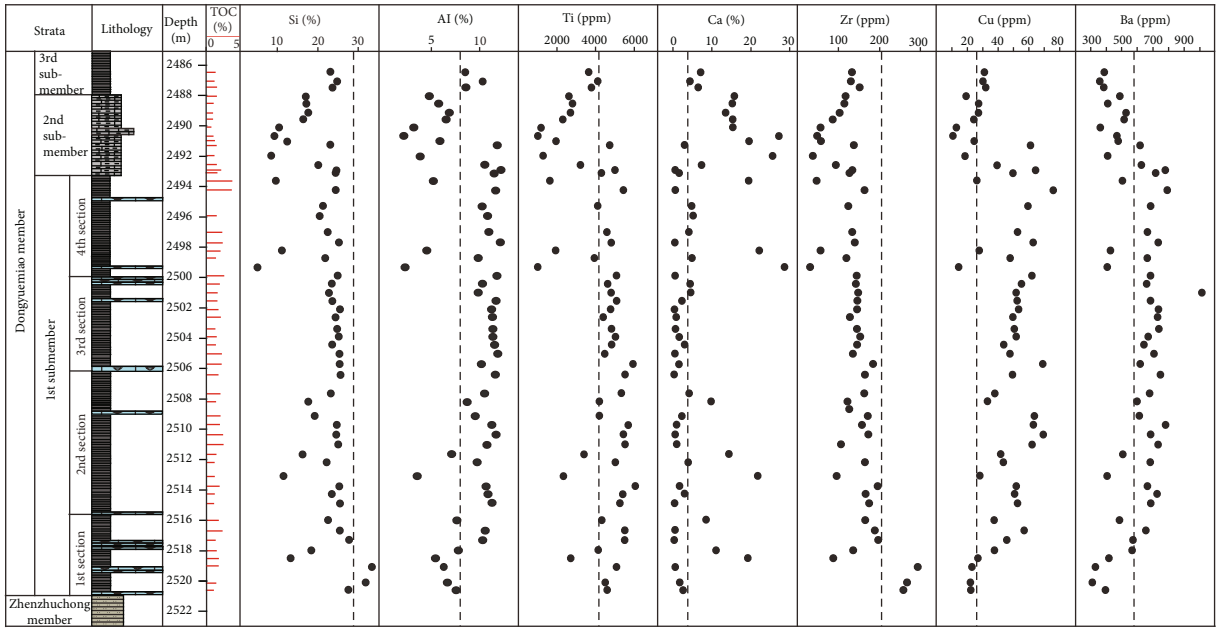


Figure 6: Environment-sensitive element concentrations for $J_1d$ from well C (1). Dashed lines refer to element contents of the upper continental crust [25].

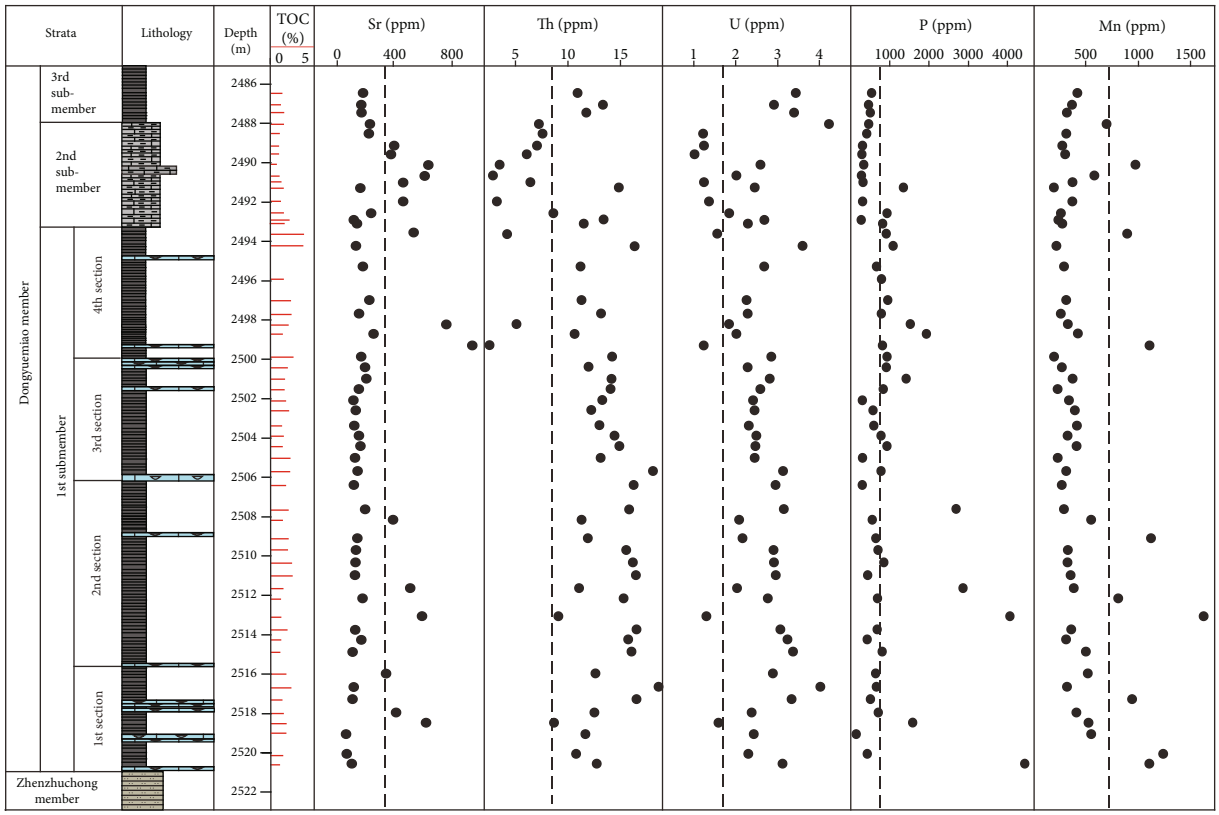


Figure 7: Environment-sensitive element concentrations for $J_1d$ from well C (2). Dashed lines refer to element contents of upper continental crust [25].

*5.3. Paleosalinity.* Paleosalinity is a critical proxy when restoring environmental condition. B and Ga were proposed to be two salinity-sensitive elements [41, 42]. Generally, the content of B and Ga in seawater is high, and the enrichment degree of B in seawater is linearly correlated with salinity. The solubility of minerals containing Ga is generally low,

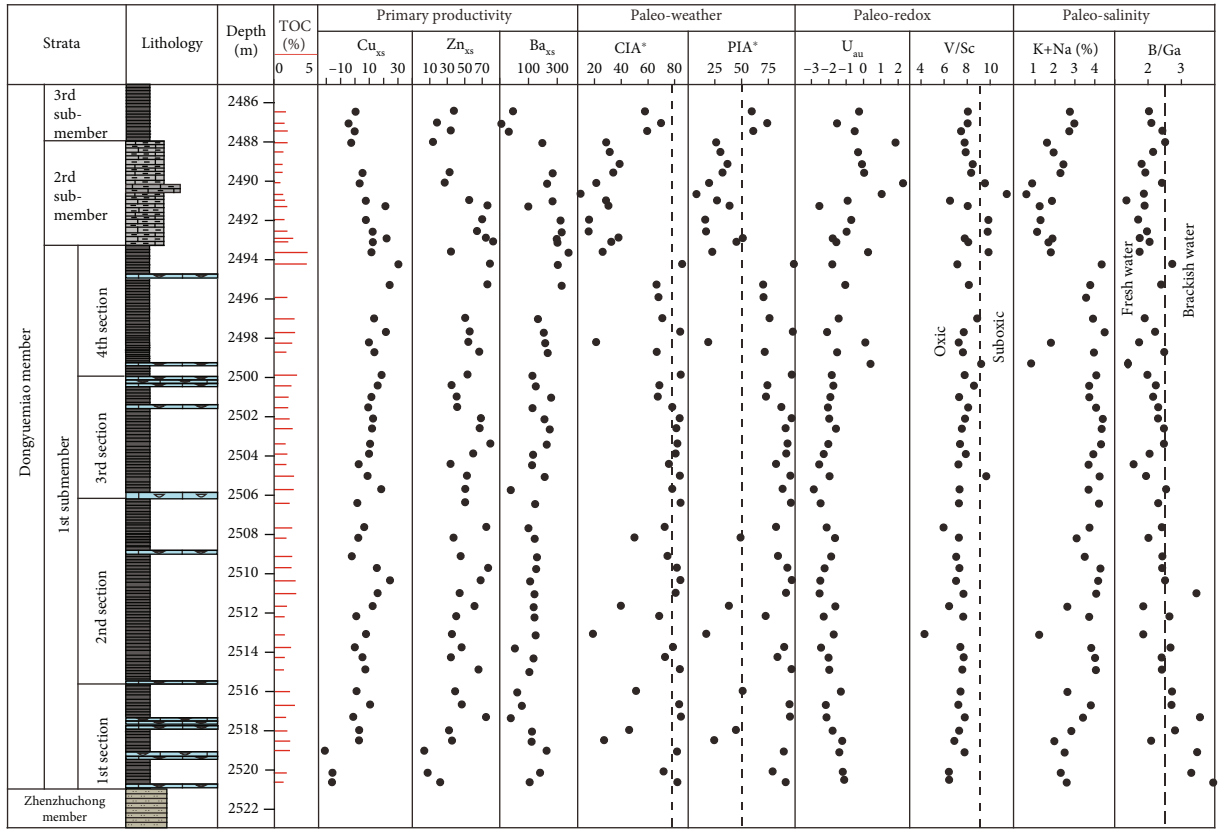


Figure 8: Environment-sensitive elemental proxies for $J_1d$ from well C. The dotted lines represent the threshold value proposed by [26].

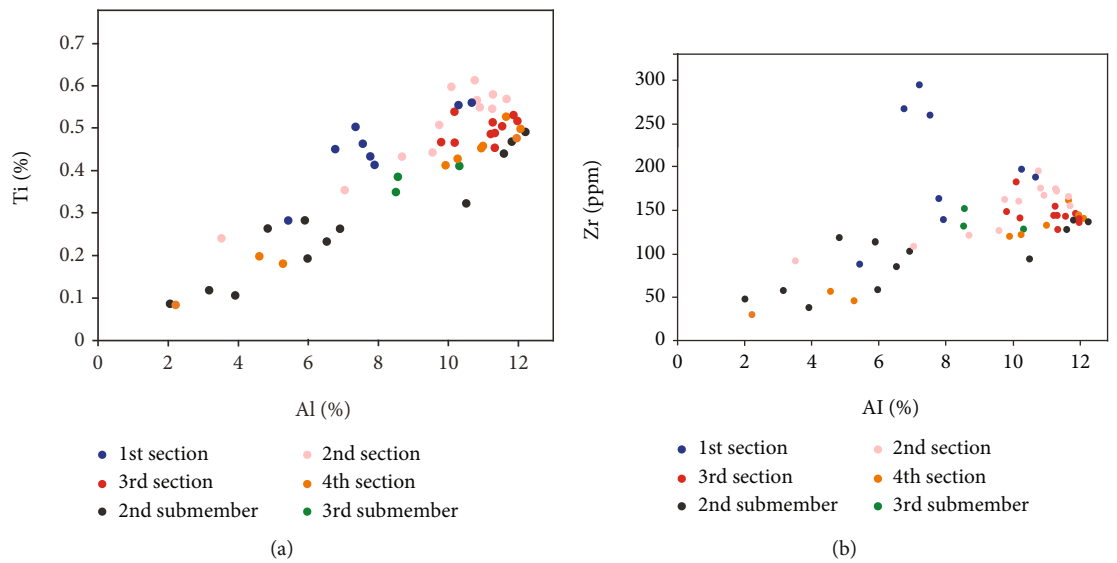


Figure 9: (a) Crossplots of Ti-Al for $J_1d$. (b) Crossplots of Zr-Al for $J_1d$.

and it is generally cleaned by particles in seawater, resulting in the concentration of Ga in seawater that is generally much lower than that in freshwater system. Therefore, the content of Ga in marine sediments is generally lower than that in continental sediments [42, 43]. Therefore, B/Ga and B contents are often used to distinguish sedimentary environments. The results suggest that the paleosalinity during deposition of 1st submember is in the range of brackish water and has a gradual decreasing trend. The paleosalinity of the 2nd submember is very similar to freshwater. The paleosalinity of the water body during the deposition of the 3rd submember was converted to brackish water.

Na and K are highly active elements in alkali metals. Usually Na and K are evenly distributed in water, and their

levels can be used to directly reflect salinity [44]. The variation trend of the (K+Na) curve is similar to that of B/Ga, suggesting the same paleosalinity variation characteristics.

*5.4. Paleoredox Conditions.* Trace element proxies including $U_{au}$, V/Sc, $U_{EF}$, and $Mo_{EF}$ were widely used to determine redox conditions for paleowater, and the smaller of these proxies reflect the higher oxidation degree, and the larger the ratio reflects the stronger reduction degree [45–47]. Authigenic Mo, authigenic U enrichment, and Mo-U covariant models have been applied to determine redox conditions and water mass limitation [36, 37, 48]. In general, the oxic condition showed little or no enrichment of authigenic U and Mo, while the anoxic conditions showed strong enrichment of authigenic U and Mo [36, 37]. The data points of each section are all located within the dysoxic zone of the unrestricted marine trend (Figure 10), and only a few data points near the suboxic zone. The variation trend of $U_{au}$ and V/Sc suggests that the bottom water is dominated by suboxic condition during the deposition period of the 4th section and 2nd submember of $J_1$d. The other sections are dominated by dysoxic lake bottom water (Figure 8).

*5.5. Paleoproductivity Proxies.* The primary productivity is proposed to be a critical factor controlling organic matter accumulation in shale [3, 4]. The strong enrichment of Ba, Cu, and Zn suggests that there was a high content of organic matter that brought it to the sediments. Subsequently, Ba, Cu, and Zn in the sediments were preserved under reducing conditions [50]. Therefore, they can be used as alternative indicators of paleoproductivity level. The results show that the 4th section and 2 submember of $J_1$d have the largest $Ba_{xs}$, $Cu_{xs}$, and $Zn_{xs}$, reflecting the highest level of paleoproductivity.

*5.5.1. Organic Matter (OM) Accumulation Mechanism.* During the $J_1$d deposition, a complete transgressive-regressive sedimentary cycle was developed within the study area [19]. The 1st section deposition represents to the early stage of the $J_1$d deposition. The eastern study area is dominated by shallow lacustrine facies (Figure 11(a)), and the lake is relatively small. The shell shoals composed of a large number of benthos can be observed on the core intervals. The water body is in oxic-dysoxic condition, which is not favorable for the preservation of OM.

During the 2nd section deposition, it experienced a strong transgressive action, and the lake area expanded significantly. The study area has the characteristics of semideep and deep lacustrine environment. Sediments of the shell shoal can trigger large-scale slumping, forming shell interlayers of gravity flow origin within semideep lacustrine environment (Figure 11(b)). During this period, the water body is relatively stable and conducive to algae and other lower aquatic organisms multiply, reflecting significantly increased primary productivity. At the same time, appropriate terrigenous influx does not cause a strong dilution effect of OM but provides more terrigenous OM. In addition, the dysoxic conditions of water bodies will also be favorable for the preservation of OM, which is favorable for OM enrichment.

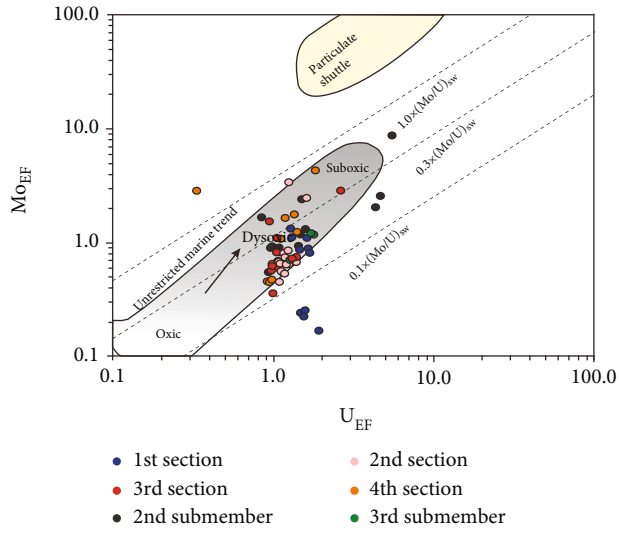


Figure 10: Authigenic Mo-U covariation patterns of $J_1$d. The diagonal dashed lines refer to the Mo/U molar ratios of the seawater (sw). Grey area refers to the "unrestricted marine" trend, characterization of depositional systems with no limited trace metal renewal. Yellow area refers to the "particulate shuttle" trend, a characterization of environments in which intense redox cycling of metals occurs within the water column [49, 50].

During the 3rd section deposition, the decrease in lake level leads to a decrease in the distribution range of deep lake areas. The water turbulence was not of benefit to phytoplankton reproduction (Figure 11(c)), and the primary productivity was at low level. During the 4th section deposition, it experienced strong lake transgression again, and the lake area reached the maximum. Meanwhile, the bottom water body of the lake was relatively stable, which was beneficial to the reproduction of aquatic phytoplankton, including algae, which was reflected in the significant increase in productivity indicators (Figure 11(d)). At the same time, appropriate terrigenous influx does not cause a strong dilution effect of OM but provides more terrigenous OM. In addition, the suboxic conditions of water body will contribute to the OM preservation and enrichment.

During the 2nd submember deposition, the study area has been restored to a semideep lacustrine environment, and gravity flow deposits were frequently developed. However, since the paleoclimate of this period converted to cold-dry climate, terrigenous influx almost stagnated, and the water body gradually changed to fresh water (Figure 11(e)). Meanwhile, the bottom water is dominated by suboxic condition. These conditions are beneficial to the reproduction and preservation of phytoplankton, by raising primary productivity. However, due to the lack of terrigenous organic matter input, the TOC content has not increased significantly. During the deposition period of the 3rd submember, the lake level gradually decreased, the lake basin shrank greatly, and the distribution range of the deep lake area gradually returned to the 1st submember deposition period. However, due to the turbulent water body and the large input of terrigenous debris (Figure 11(f)), these conditions were unfavourable for phytoplankton reproduction and the preservation of OM.

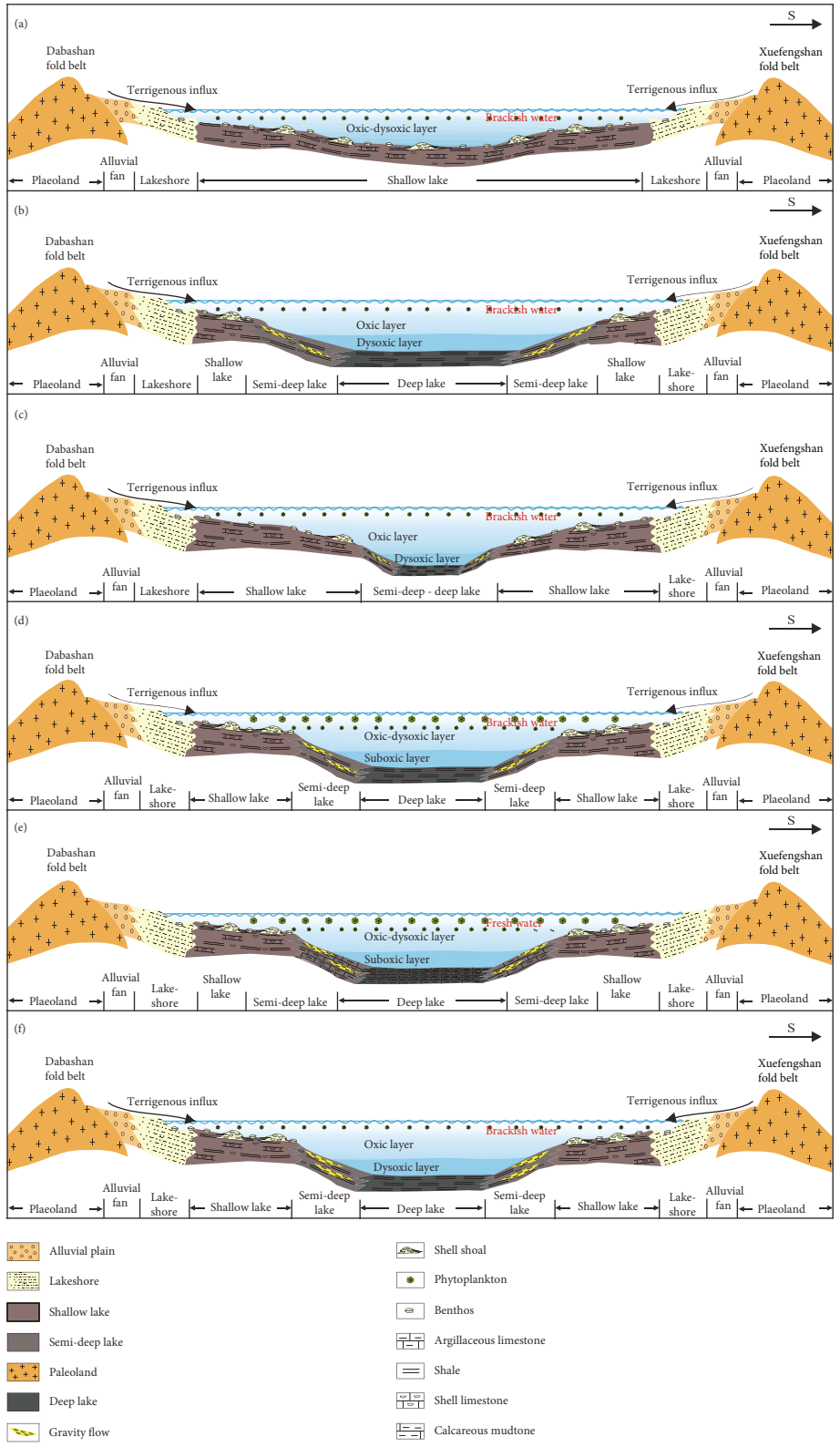


Figure 11: Controlling factors of OM enrichment mechanisms for $J_1d$ lacustrine shale. (a) 1st section of $J_1d$. (b) 2nd section of $J_1d$. (c) 3rd section of $J_1d$. (d) 4th section of $J_1d$. (e) 2nd submember of $J_1d$. (f) 3rd submember of $J_1d$.

## 6. Conclusions

(1) In 1st submember, the 1st section interval of the Jurassic Dongyuemiao Member was dominated by shallow lacustrine subfacies, while the other sections have the characteristics of semideep and deep lacustrine environment. The 2nd and 3rd submembers also have the characteristics of semideep and deep lacustrine environment

(2) The 1st submember interval of the Jurassic Dongyuemiao Member was characterized by the most warm-humid condition, strongest weathering degree, largest terrigenous influx, moderate paleoproductivity, and moderate paleoredox condition. Within this submember, the 4th section interval had the highest paleoproductivity, and the most oxygen-deficient condition in bottom water. During the period of the 2nd submember interval, the sedimentary environment turned to cold-dry climatic conditions, weak weathering degree, low terrigenous input, low paleosalinity, and high paleoproductivity

(3) Under semideep lacustrine and deep lacustrine background, terrigenous OM input played a key role in controlling OM enrichment of Dongyuemiao lacustrine shale. Moreover, the high primary productivity of lake surface water and suboxic condition of lake bottom water are also beneficial for the formation of high TOC interval in the 4th section of 1st submember

## Data Availability

The raw data supporting the conclusions of this article will be made available by the authors without undue reservation.

## Conflicts of Interest

The authors declare that they have no conflicts of interest.

## Acknowledgments

This study was funded by the National Natural Science Foundation of China (Grant No. 42272171), National Science and Technology Major Project (Grant No. 2017ZX05036), and Sinopec "Ten Dragons" Technology Project (Grant No. P21078-1).

## References

[1] C. Zou, R. Zhu, Z. Chen et al., "Organic-matter-rich shales of China," *Earth-Science Reviews*, vol. 189, pp. 51–78, 2019.

[2] Y. Gu, G. Cai, D. Hu et al., "Geochemical and geological characterization of Upper Permian Linghao formation shale in Nanpanjiang Basin, SW China," *Frontiers in Earth Science*, vol. 10, article 883146, 2022.

[3] Y. Gu, X. Li, L. Qi et al., "Sedimentology and geochemistry of the Lower Permian Shanxi formation Shan $2^3$ submember transitional shale, Eastern Ordos Basin, North China," *Frontiers in Earth Science*, vol. 10, article 859845, 2022.

[4] Y. Gu, D. Hu, Z. Wei et al., "Sedimentology and geochemistry of the Upper Permian Linghao formation marine shale, Central Nanpanjiang Basin, SW China," *Frontiers in Earth Science*, vol. 10, article 914426, 2022.

[5] K. Zhang, Y. Song, S. Jiang et al., "Mechanism analysis of organic matter enrichment in different sedimentary backgrounds: a case study of the lower Cambrian and the Upper Ordovician-Lower Silurian, in Yangtze region," *Marine and Petroleum Geology*, vol. 99, pp. 488–497, 2019.

[6] K. Zhang, Y. Song, Z. Jiang et al., "Research on the occurrence state of methane molecules in post-mature marine shales-a case analysis of the Lower Silurian Longmaxi formation shales of the upper Yangtze region in southern China," *Frontiers in Earth Science*, vol. 10, article 864279, 2022.

[7] K. Zhang, Y. Song, C. Jia et al., "Formation mechanism of the sealing capacity of the roof and floor strata of marine organic-rich shale and shale itself, and its influence on the characteristics of shale gas and organic matter pore development," *Marine and Petroleum Geology*, vol. 140, article 105647, 2022.

[8] K. Zhang, J. Peng, W. Liu et al., "The role of deep geofluids in the enrichment of sedimentary organic matter: a case study of the late Ordovician-early Silurian in the upper Yangtze region and early Cambrian in the lower Yangtze region, South China," *Geofluids*, vol. 2020, Article ID 8868638, 12 pages, 2020.

[9] Y. Fu, Y. Jiang, D. Dong et al., "Microscopic pore-fracture configuration and gas-filled mechanism of shale reservoirs in the western Chongqing area, Sichuan Basin, China," *Petroleum Exploration and Development*, vol. 48, no. 5, pp. 1063–1076, 2021.

[10] Y. Jiang, X. Liu, Y. Fu et al., "Evaluation of effective porosity in marine shale reservoir, Western Chongqing," *Acta Petrolei Sinica*, vol. 40, no. 10, pp. 1233–1243, 2019.

[11] Z. Wang, Y. Jiang, Y. Fu et al., "Characterization of pore structure and heterogeneity of shale reservoir from Wufeng formation-sublayers Long-$1_1$ in Western Chongqing based on nuclear magnetic resonance," *Earth Science*, vol. 47, no. 2, pp. 490–504, 2022.

[12] H. Li, "Research progress on evaluation methods and factors influencing shale brittleness: a review," *Energy Reports*, vol. 8, pp. 4344–4358, 2022.

[13] J. Li, H. Li, C. Yang, Y. Wu, Z. Gao, and S. Jiang, "Geological characteristics and controlling factors of deep shale gas enrichment of the Wufeng-Longmaxi formation in the southern Sichuan Basin, China," *Lithosphere*, vol. 2022, article 4737801, no. Special 12, 2022.

[14] D. Chen, J. Zhang, X. Wang, B. Lan, Z. Li, and T. Liu, "Characteristics of lacustrine shale reservoir and its effect on methane adsorption capacity in Fuxin basin," *Energy & Fuels*, vol. 32, no. 11, pp. 11105–11117, 2018.

[15] W. Han, X. Zhao, F. Jin et al., "Sweet spot evaluation and exploration practice of lacustrine shale oil of the second member of Kongdian Formation in Cangdong sag, Bohai Bay Basin," *Petroleum Exploration and Development*, vol. 48, no. 4, pp. 900–910, 2021.

[16] Z. Shu, L. Zhou, X. Li et al., "Geological characteristics of gas condensate reservoirs and their exploration and development prospect in the Jurassic continental shale of the Dongyuemiao member of Ziliujing formation, Fuxing area, eastern Sichuan Basin," *Oil & Gas Geology*, vol. 42, no. 1, pp. 212–223, 2021.

[17] G. Wei, W. Wang, L. Feng et al., "Geological characteristics and exploration prospect of black shale in the Dongyuemiao

member of lower Jurassic, the eastern Sichuan Basin, China," *Frontiers in Earth Science*, vol. 9, article 765568, 2021.

[18] Y. Shu, H. Bao, Y. Zheng et al., "Lithofacies types, assemblage characteristics, and sedimentary evolution model of lacustrine shale in Dongyuemiao formation of Fuxing area," *Frontiers in Earth Science*, vol. 9, article 772581, 2021.

[19] J. Peng, Z. Hu, D. Feng, and Q. Wang, "Sedimentology and sequence stratigraphy of lacustrine deep-water fine-grained sedimentary rocks: the lower Jurassic Dongyuemiao formation in the Sichuan Basin, Western China," *Marine and Petroleum Geology*, vol. 146, article 105933, 2022.

[20] Z. Liu, Z. Hu, G. Liu et al., "Pore characteristics and controlling factors of continental shale reservoirs in the lower Jurassic Ziliujing formation, northeastern Sichuan Basin," *Oil & Gas Geology*, vol. 42, no. 1, pp. 136–145, 2021.

[21] Z. Qiu and J. He, "Depositional environment changes and organic matter accumulation of Pliensbachian-Toarcian lacustrine shales in the Sichuan basin, SW China," *Journal of Asian Earth Sciences*, vol. 232, article 105035, 2022.

[22] J. H. Baas, J. L. Best, J. Peakall, and M. Wang, "A phase diagram for turbulent, transitional, and laminar clay suspension flows," *Journal of Sedimentary Research*, vol. 79, no. 4, pp. 162–183, 2009.

[23] E. J. Sumner, P. J. Talling, and L. A. Amy, "Deposits of flows transitional between turbidity current and debris flow," *Geology*, vol. 37, no. 11, pp. 991–994, 2009.

[24] J. Hovikoski, J. Therkelsen, L. H. Nielsen et al., "Density-flow deposition in a fresh-water lacustrine rift basin, Paleogene bach long vi graben, Vietnam," *Journal of Sedimentary Research*, vol. 86, no. 9, pp. 982–1007, 2016.

[25] S. M. McLennan, "Relationships between the trace element composition of sedimentary rocks and upper continental crust: trace element composition and upper continental crust," *Geochemistry, Geophysics, Geosystems*, vol. 2, article 2000GC000109, 2001.

[26] T. Deng, Y. Li, Z. Wang et al., "Geochemical characteristics and organic matter enrichment mechanism of black shale in the upper Triassic Xujiahe formation in the Sichuan basin: implications for paleoweathering, provenance and tectonic setting," *Marine and Petroleum Geology*, vol. 109, no. 698-716, pp. 698–716, 2019.

[27] Y. Li, T. Zhang, G. S. Ellis, and D. Shao, "Depositional environment and organic matter accumulation of Upper Ordovician-Lower Silurian marine shale in the Upper Yangtze Platform, South China," *Palaeogeography Palaeoclimatology Palaeoecology*, vol. 466, pp. 252–264, 2017.

[28] Q. Liu, P. Li, Z. Jin et al., "Preservation of organic matter in shale linked to bacterial sulfate reduction (BSR) and volcanic activity under marine and lacustrine depositional environments," *Marine and Petroleum Geology*, vol. 127, article 104950, 2021.

[29] M. L. Caplan and R. M. Bustin, "Sedimentology and sequence stratigraphy of Devonian-carboniferous strata, southern Alberta," *Bulletin of Canadian Petroleum Geology*, vol. 46, no. 4, pp. 487–514, 1998.

[30] A. E. Murphy, B. B. Sageman, D. J. Hollander, T. W. Lyons, and C. E. Brett, "Black shale deposition and faunal overturn in the Devonian Appalachian Basin: clastic starvation, seasonal water-column mixing, and efficient biolimiting nutrient recycling," *Paleoceanography*, vol. 15, no. 3, pp. 280–291, 2000.

[31] P. Bertrand, G. Shimmield, P. Martinez et al., "The glacial ocean productivity hypothesis: the importance of regional temporal and spatial studies," *Marine Geology*, vol. 130, no. 1-2, pp. 1–9, 1996.

[32] V. Rachold and H. J. Brumsack, "Inorganic geochemistry of Albian sediments from the Lower Saxony Basin NW Germany: palaeoenvironmental constraints and orbital cycles," *Palaeogeography Palaeoclimatology Palaeoecology*, vol. 174, no. 1-3, pp. 121–143, 2001.

[33] H. Nesbitt and G. Young, "Early proterozoic climates and plate motions inferred from major element chemistry of lutites," *Nature*, vol. 299, no. 5885, pp. 715–717, 1982.

[34] J. R. Price and M. A. Velbel, "Chemical weathering indices applied to weathering profiles developed on heterogeneous felsic metamorphic parent rocks," *Chemical Geology*, vol. 202, no. 3-4, pp. 397–416, 2003.

[35] Z. Liu, T. J. Algeo, X. Guo, J. Fan, X. Du, and Y. Lu, "Paleoenvironmental cyclicity in the Early Silurian Yangtze Sea (South China): Tectonic or glacio-eustatic control?," *Palaeogeography Palaeoclimatology Palaeoecology*, vol. 466, pp. 59–76, 2017.

[36] T. J. Algeo and N. Tribovillard, "Environmental analysis of paleoceanographic systems based on molybdenum- uranium covariation," *Chemical Geology*, vol. 268, no. 3-4, pp. 211–225, 2009.

[37] T. J. Algeo and J. S. Liu, "A re-assessment of elemental proxies for paleoredox analysis," *Chemical Geology*, vol. 540, article 119549, 2020.

[38] K. H. Wedepohl, "The composition of the continental crust," *Geochimica et Cosmochimica Acta*, vol. 59, no. 7, pp. 1217–1232, 1995.

[39] S. R. Taylor and S. M. McLennan, *The Continental Crust: Its Composition and Evolution*, Blackwell, Oxford, 1985.

[40] Y. Bai, Z. Liu, P. Sun et al., "Rare earth and major element geochemistry of Eocene fine-grained sediments in oil shale- and coal-bearing layers of the Meihe Basin, Northeast China," *Journal of Asian Earth Sciences*, vol. 97, no. 97, pp. 89–101, 2015.

[41] D. M. Bennett, S. C. Fritz, J. C. Holz, A. A. Holz, and V. A. Zlotnik, "Evaluating climatic and non-climatic influences on ion chemistry in natural and man-made lakes of Nebraska, USA," *Hydrobiologia*, vol. 591, no. 1, pp. 103–115, 2007.

[42] J. McAlister and K. Orians, "Calculation of river-seawater end-members and differential trace metal scavenging in the Columbia River plume," *Estuarine, Coastal and Shelf Science*, vol. 99, pp. 31–41, 2012.

[43] K. J. Orians and K. W. Bruland, "The marine geochemistry of dissolved gallium: a comparison with dissolved aluminum," *Geochimica et Cosmochimica Acta*, vol. 52, no. 12, pp. 2955–2962, 1988.

[44] H. Gao, X. Liu, P. Liu, P. Meng, L. Xiang, and G. Rao, "Paleosalinity characteristics and geological significance of the upper Bayingobi formation in Yingejing depression, Bayingebi Basin," *Geological Journal of China Universities*, vol. 28, no. 4, pp. 539–553, 2022.

[45] J. Cao, R. Yang, W. Yin, G. Hu, L. Bian, and X. Fu, "Mechanism of organic matter accumulation in residual bay environments: the early cretaceous Qiangtang Basin, Tibet," *Energy & Fuels*, vol. 32, no. 2, pp. 1024–1037, 2018.

[46] S. Liu, C. Wu, T. Li, and H. Wang, "Multiple geochemical proxies controlling the organic matter accumulation of the marine-continental transitional shale: A case study of the Upper Permian Longtan Formation, western Guizhou,

China," *Journal of Natural Gas Science and Engineering*, vol. 56, pp. 152–165, 2018.

[47] Q. He, T. Dong, S. He et al., "Sedimentological and geochemical characterization of the upper Permian transitional facies of the Longtan formation, northern Guizhou Province, Southwest China: insights into paleo-environmental conditions and organic matter accumulation mechanisms," *Marine and Petroleum Geology*, vol. 118, article 104446, 2020.

[48] T. J. Algeo and T. W. Lyons, "Mo-total organic carbon covariation in modern anoxic marine environments: implications for analysis of paleoredox and paleohydrographic conditions," *Paleoceanography*, vol. 21, no. 1, pp. 16–23, 2006.

[49] N. Tribovillard, T. J. Algeo, F. Baudin, and A. Riboulleau, "Analysis of marine environmental conditions based onmolybdenum-uranium covariation—applications to Mesozoic paleoceanography," *Chemical Geology*, vol. 324-325, pp. 46–58, 2012.

[50] N. Tribovillard, T. J. Algeo, T. Lyons, and A. Riboulleau, "Trace metals as paleoredox and paleoproductivity proxies: an update," *Chemical Geology*, vol. 232, no. 1-2, pp. 12–32, 2006.